

We are IntechOpen, the world's leading publisher of Open Access books Built by scientists, for scientists

4,800

Open access books available

122,000

International authors and editors

135M

Downloads

Our authors are among the

154

Countries delivered to

TOP 1%

most cited scientists

12.2%

Contributors from top 500 universities



WEB OF SCIENCE™

Selection of our books indexed in the Book Citation Index
in Web of Science™ Core Collection (BKCI)

Interested in publishing with us?
Contact book.department@intechopen.com

Numbers displayed above are based on latest data collected.
For more information visit www.intechopen.com



Modeling and Analysis of Molten Pool Behavior for Submerged Arc Welding Process with Single and Multi-Wire Electrodes

Dae-Won Cho

Additional information is available at the end of the chapter

<http://dx.doi.org/10.5772/intechopen.76725>

Abstract

This chapter describes the procedure of modelling and analysis of molten pool behavior for submerged arc welding process with single and multi-electrodes. As submerged arc welding process is conducted under the covered flux, it is very difficult to extract the various arc shapes and its physical models such as arc heat flux, arc pressure, electromagnetic force, droplet impingement and heat source by consumed flux. This chapter suggests the way to extract the various arc models for submerged arc welding process for single and multi-wire electrodes. As the droplet movements in submerged arc welding process are different from the arc current, this chapter tries to make the flux-wall guided droplet impingement models for low current value ($I < 500$ A) and spray droplet impingement model for high current value. In high current single electrode submerged arc welding, the molten pool flow pattern for different electrode angle and welding signal wave forms (DC and AC) are analyzed. This chapter also modeled and analyzed the molten pool behaviors for multi-wire electrodes in submerged arc welding process with an arc interaction models for different current values.

Keywords: computational fluid dynamics (CFD), submerged arc welding (SAW), molten pool flow, arc interaction, multi-wire electrode

1. Introduction

Submerged arc welding (SAW) is a very complex process that includes physical and chemical reactions. Moreover, it is very difficult to investigate the whole SAW process using numerical simulations [1–4]. However, the molten zone and heat-affected zone (HAZ) could be estimated using the finite element method (FEM) and considering just the conduction heat transfer.

Wen et al. [1] modeled multi-wire SAW of thick-wall line pipe and calculated the thermal distributions under various welding conditions. Sharma et al. [2] predicted the temperature distributions and angular distortions in single-pass butt joints using three-dimensional simulations. Mahapatra et al. [3] suggested and validated a volumetric heat source model of twin-wire SAW by using different electrode diameters and polarities. Kiran et al. [4] simulated a three-dimensional heat transfer of a V-groove tandem SAW process for various welding conditions using FEM. However, these studies with FEM only considered the heat conduction transfer in the welding process, which is insufficient to explain the curve weld bead such as fingertip penetration.

To overcome these disadvantages, computational fluid dynamics (CFD) is widely used to investigate molten pool flows and final weld beads because it makes it possible to approach the welding process more realistically [5]. Considering the importance of weld pool convection in the welding process, numerous researchers have attempted to analyze the heat transfer and fluid flow. Kim et al. [6] calculated the convective heat transfer and resultant temperature distributions for a fillet gas metal arc welding (GMAW) process. Kim et al. [7] obtained the thermal data and analyzed the molten pool flows for various driving forces in stationary gas tungsten arc welding (GTAW). However, these studies assumed that the welding process was in a quasi-steady-state. Thus it was very difficult to approximate the droplet impingent and arc variation with alternating current (AC). Therefore, it is necessary to apply a transient analysis to the welding simulation because it can detect the free surface variation during the simulation time. One transient analysis method is the volume of fluid (VOF) method, which can track the molten pool surface; therefore, the variable models from arc plasma could be implemented in the simulations. Cho et al. [8] calculated the electromagnetic force (EMF) with mapping coordinates in V-groove GTAW and GMAW, and then applied it to the numerical simulation to obtain the dynamic molten pool behavior and final weld bead using the commercial software, Flow-3D. With the advantage of VOF transient simulation, Cho et al. [9] could calculate unstable molten pool flow patterns such as humping and overflow in V-groove positional GMAW. Cho et al. [10] obtained the heat flux distribution of the arc plasma in gas hollow tungsten arc welding (GHTAW) using the Abel inversion method and applied it to the VOF model to predict the molten zone area. Additionally, a more complex welding process can also be calculated by VOF. Cho and Na [11] conducted a laser welding simulation that included the multiple reflection and keyhole formation. Moreover, Cho and Na [12] conducted the three-dimensional laser-GMA hybrid welding, which adopted the laser welding and GMAW. Han et al. [13] compared the driving forces for the weld pool dynamics in GTAW and laser welding. The VOF method could also be applied to describe the alloying element distributions and pore generation in the laser-GMA hybrid welding process [14].

The modeling and the molten pool flow analysis of SAW process are mostly conducted by Cho et al. [15–21]. Cho et al. [15] conducted molten pool analysis of SAW for single electrode for high-current ($I > 500$ A) condition with spray metal transfer droplet impingement. They considered electrode angle and wave form and modeled to analyze the molten pool behavior for single electrode direct current (DC) and alternative current (AC) welding signals. It was found that the penetration of weld bead is closely related with electrode angle and waveform of welding signal. Cho et al. [16] also found that droplet impingement of low-current ($I < 500$)

could be expected as a flux-wall guided (FWG) metal transfer using CFD simulation. They modeled FWG metal transfer with a moving cylinder and randomly directed droplet impingement. Therefore, it is possible to simulate how porosity can be trapped in the V-groove joint with a FWG metal transfer. For better productivity, the multi-electrode SAW process is proposed. Kiran et al. [17] developed physical and regression equations to predict the arc interaction and arc size as a function of the welding conditions for tandem submerged arc welding process. They modeled arc center displacements for tandem SAW under different welding conditions with a spring model. It was found that the arc center displacement of high current shifted less while that of low current shifted wider. Cho et al. [18] applied the arc interaction effect to simulate the molten pool behavior for tandem SAW process. They compared the various molten pool flow patterns where the combinations of the welding signals were different. Moreover, they found that the direction of droplet impingement was very important to expect the welding penetration. Kiran et al. [19] analyzed the temperature histories of tandem SAW CFD simulations within the same heat input. They compared cooling times from 800 to 500°C and volume fractions for different welding conditions and they found that molten pool behavior played an important role to decide the volume fraction and micro hardness. Cho et al. [20] analyzed the flux consumption rate for tandem SAW process where the heat inputs were the same except the combination of welding signals (current and voltage). They found that the arc interaction, droplet impingement direction and metal transfer mode (spray & FWG) affected the overall flux consumption rates. Kiran et al. [21] modeled three wire SAW molten pool simulation which considered arc center displacement and droplet impingement with a physical approach and then analyzed molten pool flow patterns. This chapter briefly introduces the contents how to model and analyze the molten pool behaviors from numerical simulations for single and multi-wire SAW process.

2. Modeling of molten pool behavior for SAW process

2.1. CFD modeling for single electrode

Figure 1 shows a schematic diagram of SAW to allow the following characteristics to be understood [15]: (a) the flux and molten slag cover the overall weld bead and, (b) the fabricated flux wall protects the flux cavity.

Although it is very difficult to observe the metal transfer of SAW, some previous studies succeeded in capturing the motion of a droplet in SAW. Franz [22] and Van Adrichem [23] observed the metal transfer through a ceramic tube using a X-ray cinematography and found that drops travel in free flight to the weld pool, or they may project sideways to collide with the molten flux wall. This metal transfer in SAW is the so-called flux-wall guided (FWG) transfer, as shown in **Figure 2**.

During the SAW process, a small portion of the flux is melted and consumed. Chandel [24] found that the flux consumption relies upon three sources: (a) conduction from the molten metal, (b) radiation from arc and (c) resistance heating of the slag. However, their individual

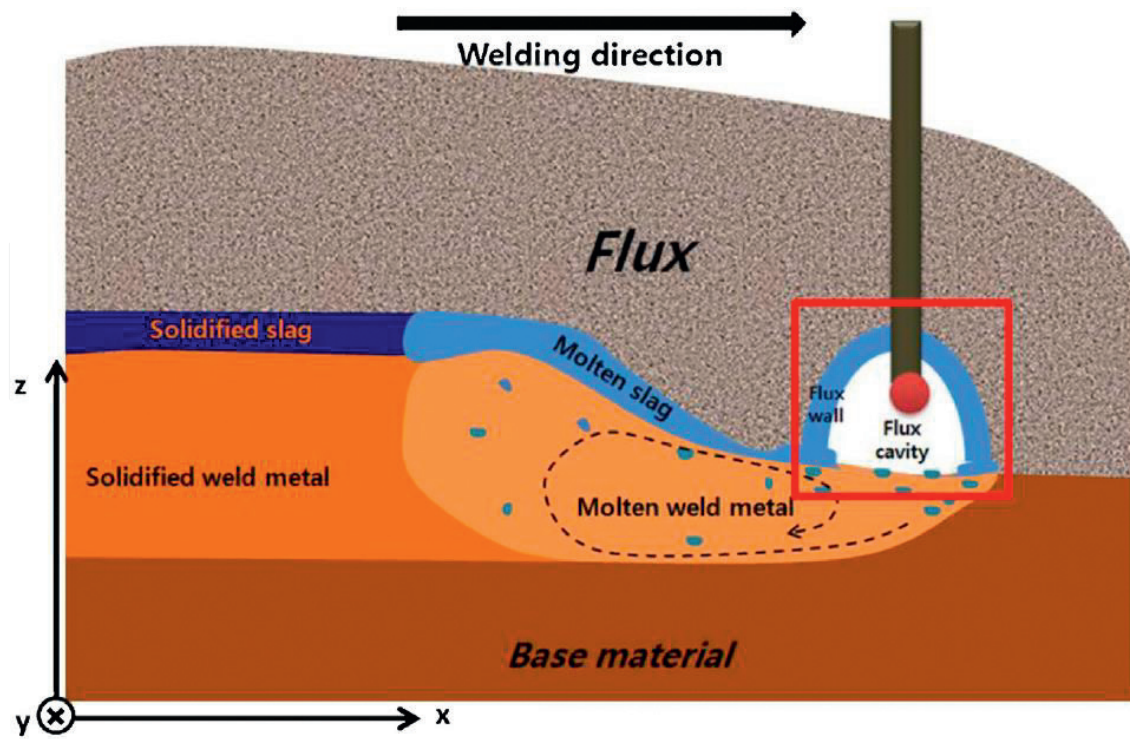


Figure 1. Schematic of SAW [15].

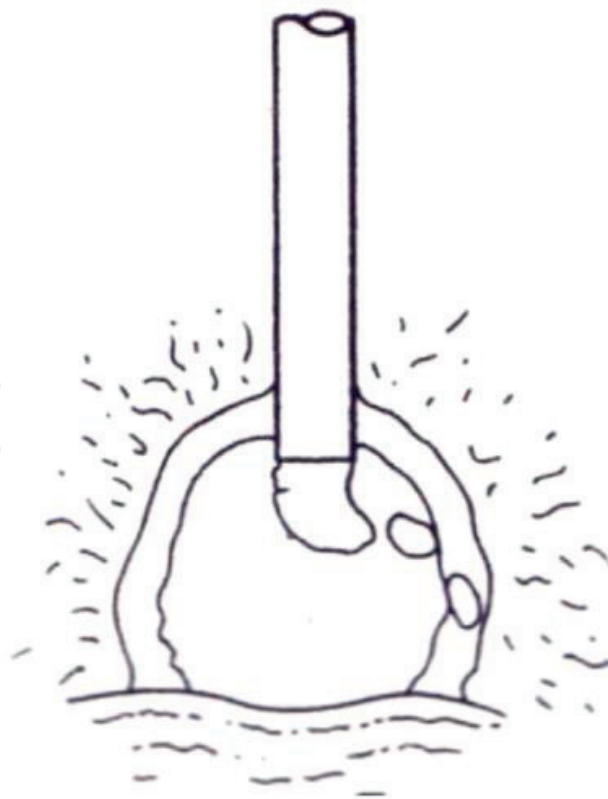


Figure 2. FWG transfer in SAW [15].

contributions to flux consumption are still unclear. In any case, the total flux consumption can be calculated by measuring the mass of the flux used. Renwick and Patchett [25] analyzed the relations between welding parameters and the flux consumption and found that flux consumption initially increased with increasing current, reached a maximum, and then decreased. Chandel [24] also measured the flux consumption of SAW with various welding parameters and showed that the flux consumption reached a peak value at 500 A and decreased at higher currents, as shown in **Figure 3** [15]. This decrease at a high current is a result of the increasing current causing the droplet size to decrease. Therefore, the contact area between the droplet and the flux-wall could be decreased, as shown in **Figure 4**. In short, FWG transfer is difficult to observe at high current and the spray mode of transfer can be expected to be considered in high current SAW [15].

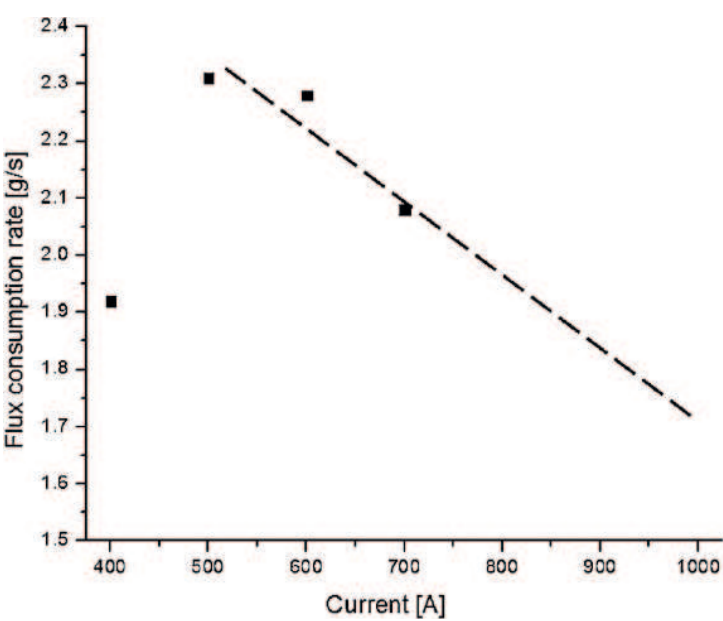


Figure 3. Current vs. flux consumption rate in single DC [15].

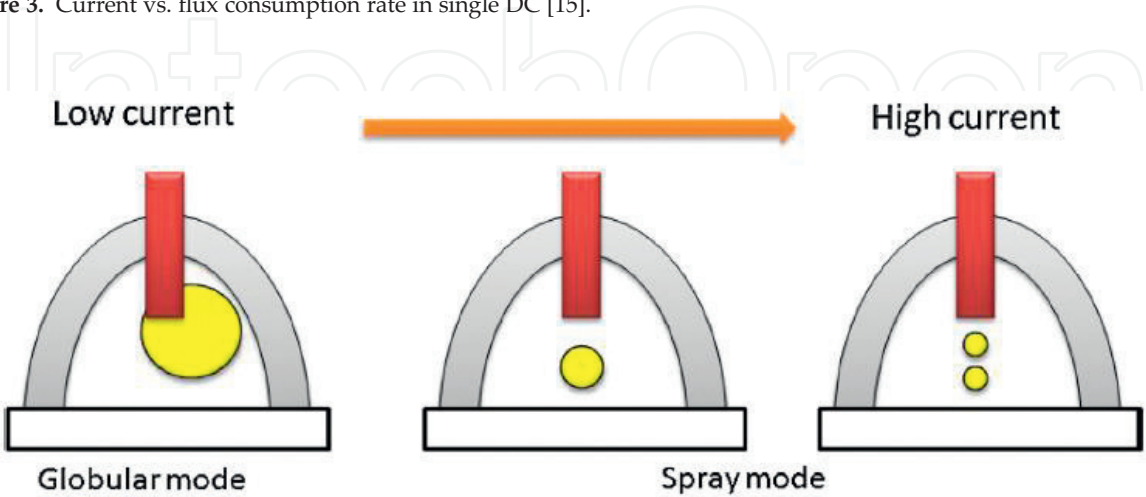


Figure 4. Expected metal transfer in single SAW process [15].

2.1.1. Governing equations

The governing equations in the CFD simulation of a weld pool involve the mass conservation equation, momentum conservation equation (Navier-Stokes equations), and energy conservation equation. The time step used in the numerical simulation is 0.00001 s. To describe the molten pool behavior, the commercial package, Flow-3D was widely used [15, 16, 18, 21] (**Table 1**).

- Momentum equation

$$\frac{\partial \vec{V}}{\partial t} + \vec{V} \cdot \nabla \vec{V} = -\frac{\nabla p}{\rho} + \nu \nabla^2 \vec{V} + \frac{\dot{m}_s}{\rho} (\vec{V}_s - \vec{V}) + f_b \quad (1)$$

- Mass conservation equation

$$\nabla \cdot \vec{V} = \frac{\dot{m}_s}{\rho} \quad (2)$$

- Energy equation

$$\frac{\partial h}{\partial t} + \vec{V} \cdot \nabla h = \frac{1}{\rho} \nabla \cdot (k \nabla T) + \dot{h}_s, \quad (3)$$

where

$$\begin{aligned} h &= \rho_s C_s T & (T \leq T_s) \\ h &= h(T_s) + h_{sl} \frac{T - T_s}{T_l - T_s} & (T_s < T \leq T_l) \\ h &= h(T_l) + \rho_l C_l (T - T_l) & (T_s < T \leq T_l) \end{aligned} \quad (4)$$

- VOF equation

$$\frac{\partial F}{\partial t} + \nabla \cdot (\vec{V} F) = \dot{F}_s \quad (5)$$

2.1.2. Boundary conditions

There is no heat loss from the radiation, convection and evaporation on the molten pool surface because slag and flux cover the overall weld bead as shown in **Figure 1**. In SAW, the heat is input from the slag to the molten pool and lost from the molten pool to the slag. However, the summation of the heat input and heat loss can be regarded as the slag heat transfer (q_s), and the energy boundary condition in equation (6) is used [15, 16, 18, 21].

$$k \frac{\partial T}{\partial \vec{n}} = q_a + q_{slag_input} - q_{slag_loss} = q_a + q_s. \quad (6)$$

Symbol	Nomenclature	Symbol	Nomenclature
ρ	Density, (solid:7.8, liquid:6.9, g/cm ³)	p_A	Arc pressure
\vec{V}	Velocity vector	R_c	Radius of the surface curvature
ν	Kinematic viscosity	γ	Surface tension
\dot{m}_s	Mass source of droplet	r_w	Radius of wire, 2.0 mm
h	Enthalpy	r_d	Radius of droplet, 2.1 mm
\dot{h}_s	Enthalpy source of droplet	WFR	Wire feed rate
\vec{V}_s	Velocity vector for mass source	C_s	Specific heat of liquid, 7.32x 10 ⁶ erg/g s K
f_b	Body force	C_p	Specific heat
h_s	Enthalpy of solid	T_o	Room temperature, 298 K
h_{sl}	Enthalpy between solid and solid	η_s	Slag efficiency of SAW
T_s	Solidus temperature, 1768 K	η_d	Droplet efficiency of SAW
T_l	Liquidus temperature, 1798 K	\dot{m}_f	Flux consumption (g/s)
F	Fraction of fluid	x_0, y_0	Location of the electrode center in x and y directions
\dot{F}_s	Volume source of droplet	x_1, y_1	Location of the arc center in x and y directions
k	Thermal conductivity	J_0	First kind of Bessel function of zero order
\vec{n}	Normal vector to free surface	μ_0	Permeability of vacuum, 1.26 × 10 ⁶ H/m
q_a	Heat input from arc plasma	μ_m	Material permeability, 1.26 × 10 ⁶ H/m
q_d	Heat input from droplet	J_z	Vertical component of the current density
q_{slag_input}	Heat transfer from slag to molten pool	J_r	Radial component of the current density
q_{slag_loss}	Heat transfer from slag to molten pool	B_θ	Angular component of the magnetic field
η_a	Arc efficiency of SAW	σ_x, σ_y	Effective radius of the arc in x-direction and y-direction
I	Current	Γ_s	Surface excess at saturation
V	Voltage	\bar{R}	Universal gas constant
F_b	Buoyancy force	k_1	Constant related to the entropy of segregation
γ_m^0	Surface tension of pure metal at melting point	a_1	Weight percent of sulfur
A	Negative surface tension gradient for pure metal	I_L, I_T	Current of leading and trailing electrodes
ΔH^0	Standard heat of adsorption	l_L, l_T	Arc length of leading and trailing leading electrodes
X_L, X_T	Arc center position of x-direction for leading and trailing electrodes	β_n^{ij}	Coefficients of effective radius model
$B_{\theta L}, B_{\theta T}$	Angular component of the magnetic field for leading and trailing electrodes	d	Distance between leading and trailing electrode
σ_{RL}, σ_{FL}	Rear and front effective radii of leading arc in x-direction	J_{zL}, J_{zT}	Vertical component of the current density for leading and trailing arcs

Symbol	Nomenclature	Symbol	Nomenclature
σ_{RT}, σ_{FT}	Rear and front effective radii of trailing arc in x-direction	J_{rL}, J_{rT}	Radial component of the current density for leading and trailing arcs
q_{aL}, q_{aT}	Arc heat flux for leading and trailing electrodes	P_{aL}, P_{aT}	Arc heat flux for leading and trailing electrodes

Table 1. Properties and constants used in simulations.

Previous studies found that the thermal efficiency of SAW is between 0.90 and 0.99, and many studies have used a thermal efficiency of 0.95 in numerical simulations [15, 16, 18, 21]. It is reasonable to use total thermal efficiency of 0.95 with the heat transfer from the arc plasma, droplets, and molten slag to the weld pool [15, 16, 18, 21].

$$\eta_a = \frac{q_a + q_d + q_s}{VI} \approx 0.95 \quad (7)$$

The pressure boundary on the free surface is applied as follows:

$$p = p_A + \frac{\gamma}{R_c}. \quad (8)$$

- Droplet model

The droplet efficiency relies on the wire feed rate and it is possible to be calculated using Eqs. (9) to (11). The droplet efficiency can be varied from the wire feed rate and welding signals [15, 16, 18, 21].

$$f_d = \frac{3r_w^2 WFR}{4r_d^3} \quad (9)$$

$$q_d = \frac{4}{3} \pi r_d^3 \rho [C_s(T_s - T_o) + C_l(T_d - T_s) + h_{sl}] f_d, \quad (10)$$

$$\eta_d = \frac{q_d}{VI}. \quad (11)$$

For the high current ($I > 500$ A), some studies proved that spray mode of metal transfer, which is very similar to droplet impingement of GMAW, can be considered as a droplet impingement model [15, 18]. However, the metal transfer of the low current ($I < 500$ A) can be assumed as FWG metal transfer as shown in **Figure 5** [16].

- Slag heat source model

Cho et al. [15, 16, 18]. used a slag heat source model that considers the flux consumption rate, and they assumed that the distribution of the slag heat input to the material surface would be an elliptical ring as shown in **Figure 6**. The slag heat source model can be calculated from equation (12) to (14).

$$\eta_s = \frac{\dot{m}_f C_{pf} (T_{m,flux} - T_0)}{VI} \quad (12)$$

$$r_e = \sqrt{(x - x_0)^2 \left(\frac{\sigma_y}{\sigma_x} \right)^2 + (y - y_0)^2} \quad (13)$$

if $R_a < r_e \leq R_b$ then,

$$q_s = \frac{\eta_s VI}{\pi(R_b^2 - R_a^2)}, \text{ where } R_a = 3\sigma_q, R_b = R_a + 3.0mm \quad (14)$$

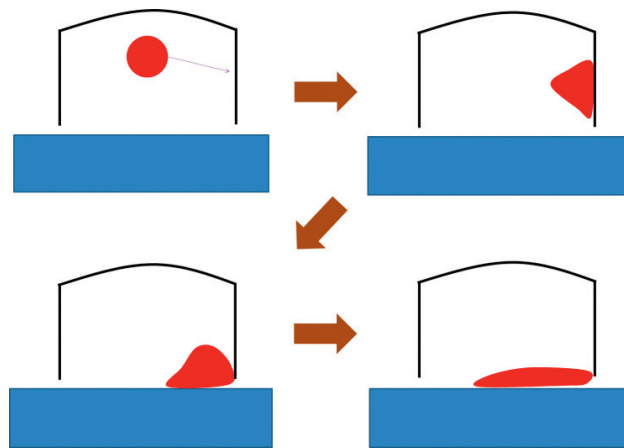


Figure 5. Schematic of droplet impingement on the wall to describe FWG transfer [16].

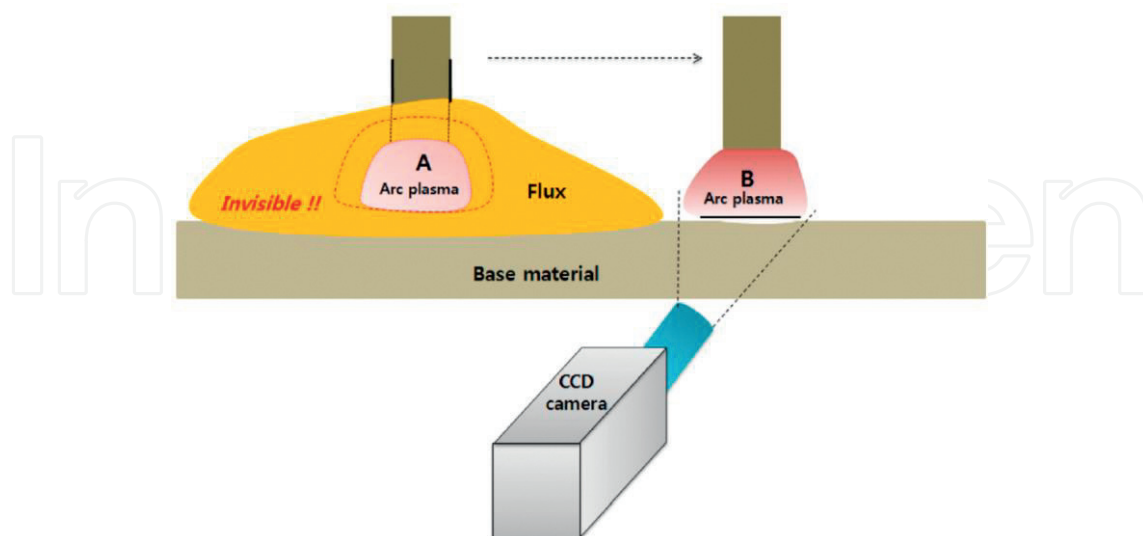


Figure 6. Process acquiring the arc plasma image [15].

- Arc heat source model

The actual arc plasma shape of SAW is very difficult to determine. Therefore, several studies assume some conditions to obtain the arc heat flux distributions [15].

- The shape of the arc plasma inside the flux (A) is very similar to the arc plasma outside the flux (B) that just escaped (within 50 ms) as shown in **Figure 6**.
- The metal vapor in the arc plasma root is neglected.

Therefore, it is reasonable to apply the elliptically symmetric Gaussian arc heat flux model in Eq. (15).

$$q_A(x, y) = \eta_A \frac{VI}{2\pi\sigma_x\sigma_y} \exp \left(-\frac{(x-x_1)^2}{2\sigma_x^2} - \frac{(y-y_1)^2}{2\sigma_y^2} \right) \quad (15)$$

- Arc pressure model

Due to the physical relationship, the effective radii of the arc heat flux and arc pressure are the same each other [10]. The resultant arc pressure model can be described in Eq. (16).

$$P_A(x, y) = \frac{\mu I^2}{4\pi^2\sigma_x\sigma_y} \exp \left(-\frac{(x-x_1)^2}{2\sigma_x^2} - \frac{(y-y_1)^2}{2\sigma_y^2} \right) \quad (16)$$

2.1.3. Electromagnetic force

In the arc welding process, Kou and Sun [26] found that the current density and self-induced magnetic field should be used to calculate the EMF in the molten pool. In the molten slag of a high current SAW process, however, Cho et al. [15, 16, 18] ignored the current flow effect in the molten slag because the magnitude of the current in the molten slag is tiny compared to the total current. Therefore, due to the physical relationship, the effective radius of electromagnetic force (EMF) model could be the same with that of the arc pressure and arc heat flux models [10]. For the elliptically symmetric distribution, EMF model can be calculated as follows:

$$k_1 = \frac{\sigma_y}{\sigma_x}, \quad (x-x_1)^2 + \frac{(y-y_1)^2}{k_1^2} = r_a^2 \quad (17)$$

$$J_z = \frac{I}{2\pi} \int_0^\infty \lambda J_0(\lambda r_a) \exp(-\lambda^2 \sigma_r^2 / 4d_a) \frac{\sinh[\lambda(c-z)]}{\sinh(\lambda c)} d\lambda \quad (18)$$

$$J_r = \frac{I}{2\pi} \int_0^\infty \lambda J_1(\lambda r_a) \exp(-\lambda^2 \sigma_r^2 / 4d) \frac{\cosh[\lambda(c-z)]}{\sinh(\lambda c)} d\lambda \quad (19)$$

$$B_\theta = \frac{\mu_m I}{2\pi} \int_0^\infty J_1(\lambda r_a) \exp(-\lambda^2 \sigma_a^2 / 4d) \frac{\sinh[\lambda(c-z)]}{\sinh(\lambda c)} d\lambda \quad (20)$$

$$F_x = -J_z B_\theta \frac{x}{r_a} \quad (21)$$

$$F_y = -J_z B_\theta \frac{y}{r_a} \quad (22)$$

$$F_z = J_z B_\theta. \quad (23)$$

2.1.4. Other models

The surface tension and buoyancy force models are not affected by the arc plasma distribution [14]. The buoyancy force can be modeled by the Boussinesq approximation and then expressed in Eq. (24).

$$F_b = \rho g \beta (T - T_0) \quad (24)$$

A surface tension model that Sahoo et al. [27] developed for a binary Fe-S system is used to model the Marangoni flow. Thus, the surface tension can be expressed in Eq. (25)

$$\gamma(T) = \gamma_m^0 - A(T - T_m) - \bar{R}T_s \ln \left(1 + k_1 a_i e^{-\Delta H^0 / \bar{R}T} \right) \quad (25)$$

2.2. CFD modeling for multi-wire electrodes

For the better productivity, many industries applied two-wire or multi-electrode tandem SAW process. When the multi-wire electrodes are used, the arc shapes and the arc center positions are changed due to electromagnetic forces of arc plasma as shown in **Figure 7**.

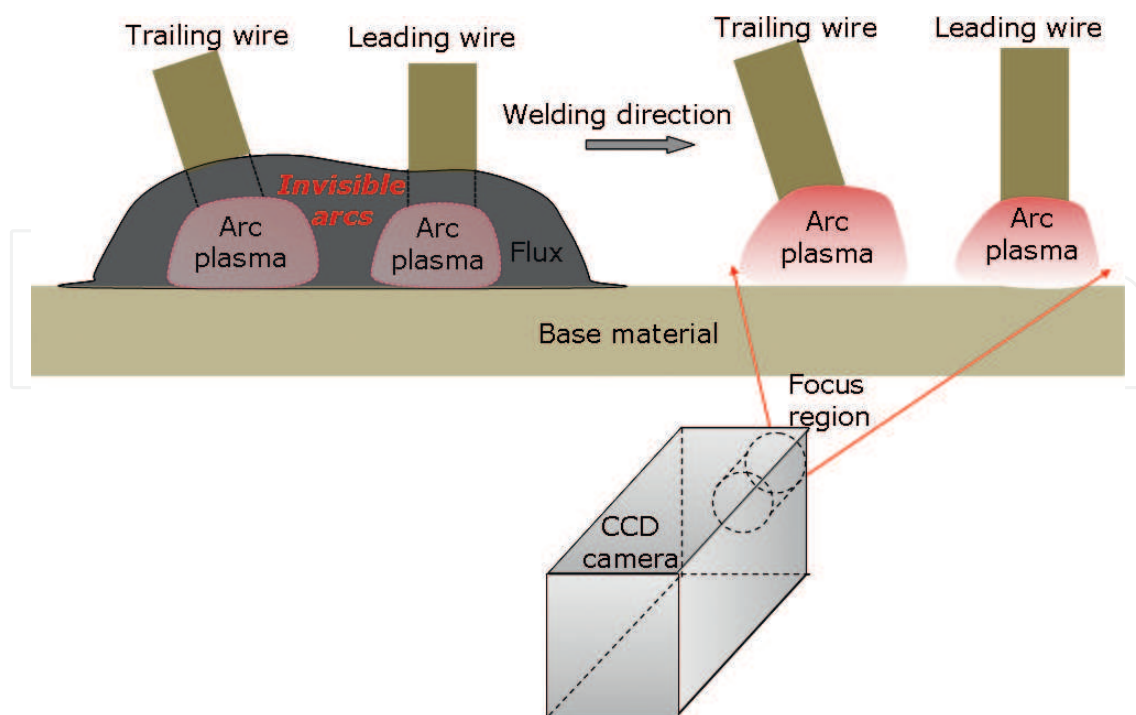


Figure 7. Schematic representation of the arc images acquisition method [17].

$$X_L = C_1 \left(\frac{I_T}{I_L} \right) \left(\frac{l_L^2}{d} \right) \quad (26)$$

$$X_T = C_2 \left(\frac{I_L}{I_T} \right) \left(\frac{l_T^2}{d} \right) \quad (27)$$

$$\sigma_{ij} = \beta_0^{ij} + \beta_1^{ij} I_j + \beta_2^{ij} V_j + \beta_3^{ij} X_j + \beta_4^{ij} I_j^2 + \beta_5^{ij} V_j^2 + \beta_6^{ij} X_j^2 + \beta_7^{ij} I_j V_j + \beta_8^{ij} V_j X_j + \beta_9^{ij} I_j X_j \quad (28)$$

2.2.1. Arc interaction model

Figure 7 illustrates the procedure followed to capture the arc images. The procedure to capture the arc images of multi-wire SAW process are very similar to single wire SAW process. Initially, the leading and trailing arcs are completely submerged under the granular flux, and a CCD camera starts to record side images of the arcs at a sampling rate of 1 kHz from the instant both the arcs come out of the flux. Kiran et al. [17, 21] considered the physical models for the arc center displacement and arc shape factors in two-wire and three wire tandem SAW process. From Eqs. (26) and (27), it is possible to expect that the higher current arc plasma is more stable than the lower current arc plasma. Additionally, the lower current arc plasma can be shifted more due to the arc interaction effect with AC welding signal. Kiran et al. [17] also proposed the effective radius of arc plasma model (27), where the welding current and voltage values are used.

2.2.2. Boundary conditions

The boundary conditions of single wire SAW from equation (6) to (8) are the same with that of multi-wire SAW process. However, two arc plasmas were used in the simulation so the arc heat source models, arc pressure, EMF models are different from those of the single wire model.

- Arc heat source model

As two arc plasmas were used in the simulations, two Gaussian asymmetric arc heat sources model, which contains different temperature distributions for the front and rear part in Eqs. (29) and (30). Therefore, Cho et al. [18] adopted the resultant effective radius to describe the Gaussian asymmetric arc models with DC and AC welding signals.

$$\begin{aligned} \text{if } x \leq x_0 \text{ then, } q_{aL}(x, y) &= \frac{\eta_a V_L I_L}{2\pi\sigma_{AL}^2} \exp \left(-\frac{(x - x_0)^2}{2\sigma_{RL}^2} - \frac{y^2}{2\sigma_{AL}^2} \right) \\ \text{if } x > x_0 \text{ then, } q_{aL}(x, y) &= \frac{\eta_a V_L I_L}{2\pi\sigma_{AL}^2} \exp \left(-\frac{(x - x_0)^2}{2\sigma_{FL}^2} - \frac{y^2}{2\sigma_{AL}^2} \right) \end{aligned} \quad (29)$$

$$\begin{aligned} \text{if } x \leq x_1 \text{ then, } q_{aT}(x, y) &= \frac{\eta_a V_T I_T}{2\pi\sigma_{AT}^2} \exp \left(-\frac{(x - x_0)^2}{2\sigma_{RT}^2} - \frac{y^2}{2\sigma_{AT}^2} \right) \\ \text{if } x > x_1 \text{ then, } q_{aT}(x, y) &= \frac{\eta_a V_T I_T}{2\pi\sigma_{AT}^2} \exp \left(-\frac{(x - x_0)^2}{2\sigma_{FT}^2} - \frac{y^2}{2\sigma_{AT}^2} \right) \end{aligned} \quad (30)$$

- Arc pressure model

The distribution of arc pressure model is the same with that of arc heat source model [10]; therefore, arc pressure model can be derived in equation (31) and (32).

$$\text{if } x \leq x_0 \text{ then, } P_{aL}(x, y) = \frac{\mu_0 I_L^2}{4\pi^2 \sigma_{AL}^2} \exp \left(-\frac{(x - x_0)^2}{2\sigma_{RL}^2} - \frac{y^2}{2\sigma_{AL}^2} \right) \quad (31)$$

$$\text{if } x > x_0 \text{ then, } P_{aL}(x, y) = \frac{\mu_0 I_L^2}{4\pi^2 \sigma_{AL}^2} \exp \left(-\frac{(x - x_0)^2}{2\sigma_{FL}^2} - \frac{y^2}{2\sigma_{AL}^2} \right)$$

$$\text{if } x \leq x_1 \text{ then, } P_{aT}(x, y) = \frac{\mu_0 I_T^2}{4\pi^2 \sigma_{AT}^2} \exp \left(-\frac{(x - x_0)^2}{2\sigma_{RT}^2} - \frac{y^2}{2\sigma_{AT}^2} \right) \quad (32)$$

$$\text{if } x > x_1 \text{ then, } P_{aT}(x, y) = \frac{\mu_0 I_T^2}{4\pi^2 \sigma_{AT}^2} \exp \left(-\frac{(x - x_0)^2}{2\sigma_{FT}^2} - \frac{y^2}{2\sigma_{AT}^2} \right)$$

- Slag heat source model

Slag heat source model in the two-wire SAW process are the same as that of single wire SAW process.

- Droplet model

Kiran et al. [17] found that the molten droplet is directed to the arc center when it is just detached. Moreover, the direction of the droplet could not be changed during the free flight. Cho et al. [18] consider that physical phenomena and then applied to the numerical simulation as shown in **Figures 8 and 9**.

The droplet efficiency relies on the wire feed rate and it is possible to be calculated using equation (9) to (11). The droplet efficiency can be varied from the wire feed rate and welding signals [15, 16, 18, 21].

2.2.3. EMF model

EMF can be induced from the two different arc plasmas; therefore EMF model used in the two-wire SAW process can be followed [18]:

$$J_{zL} = \frac{I}{2\pi} \int_0^\infty \lambda J_0(\lambda r_a) \exp(-\lambda^2 \sigma_{AL}^2 / 4d_a) \frac{\sinh[\lambda(c - z)]}{\sinh(\lambda c)} d\lambda \quad (33)$$

$$J_{rL} = \frac{I}{2\pi} \int_0^\infty \lambda J_1(\lambda r_a) \exp(-\lambda^2 \sigma_{AL}^2 / 4d_a) \frac{\cosh[\lambda(c - z)]}{\sinh(\lambda c)} d\lambda \quad (34)$$

$$B_{\theta L} = \frac{\mu_m I_L}{2\pi} \int_0^\infty J_1(\lambda r_a) \exp(-\lambda^2 \sigma_{AL}^2 / 4d_a) \frac{\sinh[\lambda(c - z)]}{\sinh(\lambda c)} d\lambda \quad (35)$$

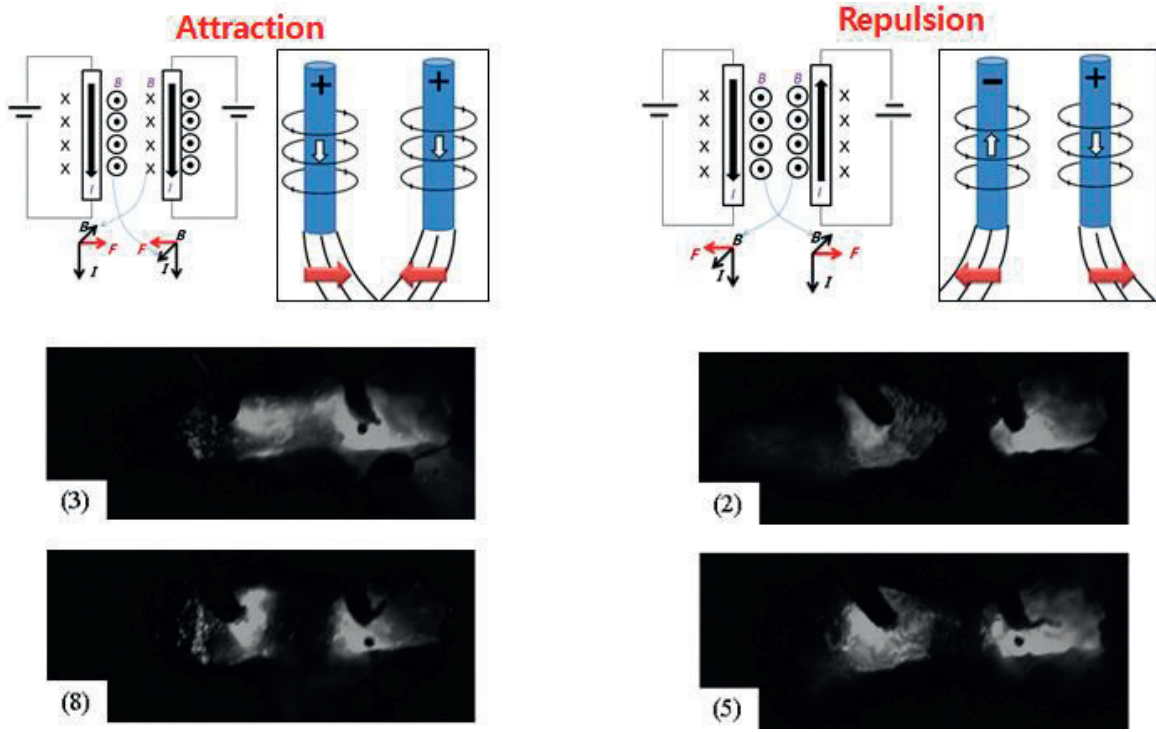


Figure 8. Arc interaction effect of the two wire tandem SAW [17, 28].

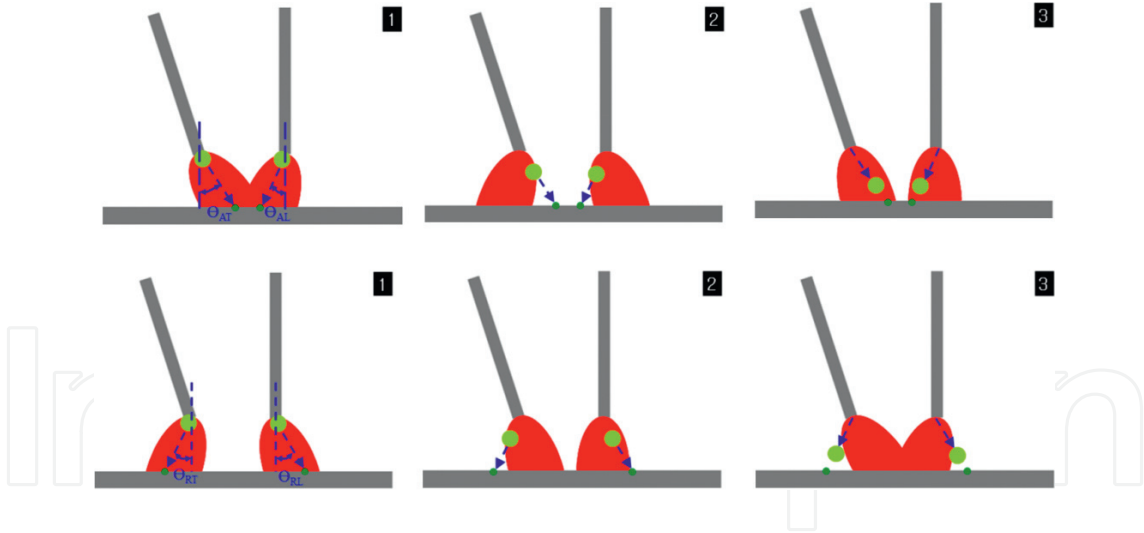


Figure 9. Droplet flights due to the arc interaction effect in two wire SAW process [18].

$$F_{rL} = J_{zL} B_{\theta L} \quad (36)$$

$$F_{zL} = J_{rL} B_{\theta L} \quad (37)$$

$$J_{zT} = \frac{I}{2\pi} \int_0^{\infty} \lambda J_0(\lambda r_a) \exp(-\lambda^2 \sigma_{AT}^2 / 4d_a) \frac{\sinh[\lambda(c-z)]}{\sinh(\lambda c)} d\lambda \quad (38)$$

$$J_{rT} = \frac{I}{2\pi} \int_0^{\infty} \lambda J_1(\lambda r_a) \exp(-\lambda^2 \sigma_{AT}^2 / 4d_a) \frac{\cosh[\lambda(c-z)]}{\sinh(\lambda c)} d\lambda \quad (39)$$

$$B_{\theta T} = \frac{\mu_m I_T}{2\pi} \int_0^{\infty} J_1(\lambda r_a) \exp(-\lambda^2 \sigma_{AT}^2 / 4d_a) \frac{\sinh[\lambda(c-z)]}{\sinh(\lambda c)} d\lambda \quad (40)$$

$$F_{rT} = J_{zT} B_{\theta T} \quad (41)$$

$$F_{zT} = J_{rT} B_{\theta T} \quad (42)$$

2.2.4. Other models

The same surface tension and buoyance force models in equation (24) and (25) are applied.

3. Simulation results for SAW process

3.1. Single wire SAW process

3.1.1. Spray mode of metal transfer

- Single DC

Cho et al. [15] simulated the molten pool behaviors for single DC SAW process which compared the molten pool behaviors for different electrode angles as shown in **Figure 10**. They found that electrode angle plays an important role to form the bead shapes such as penetration and bead width.

When the negative electrode angle is applied, the penetration of weld bead increases deeper because the droplet impingement direction is very similar to the molten pool circulation. Thus the momentum can be transferred sufficiently to the weld pool. Specifically, the molten pool flows downward and backward in the dotted box between droplet generations (**Figure 11(a)** and **(b)**) and then forms a sharp and deep penetration on a transverse cross-section by convection heat transfer as shown in **Figure 12(a)**. However, the positive electrode angle induces

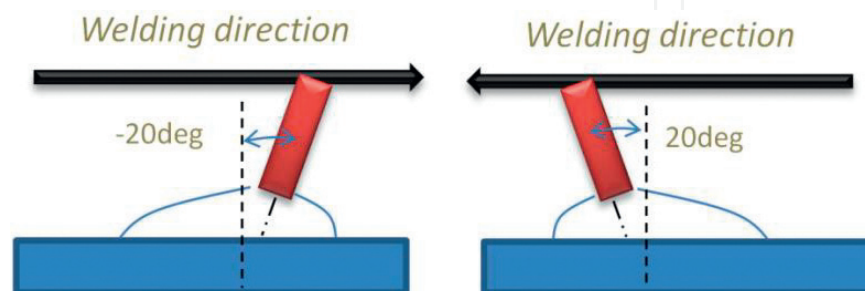


Figure 10. Electrode angle used in the simulation [28].

somewhat different flow patterns because the droplet impingement direction does not match the molten pool direction as shown in **Figure 13(a)** and **(b)**. Therefore, less momentum from the droplet impingement can be transferred in positive electrode angle compared to negative electrode angle.

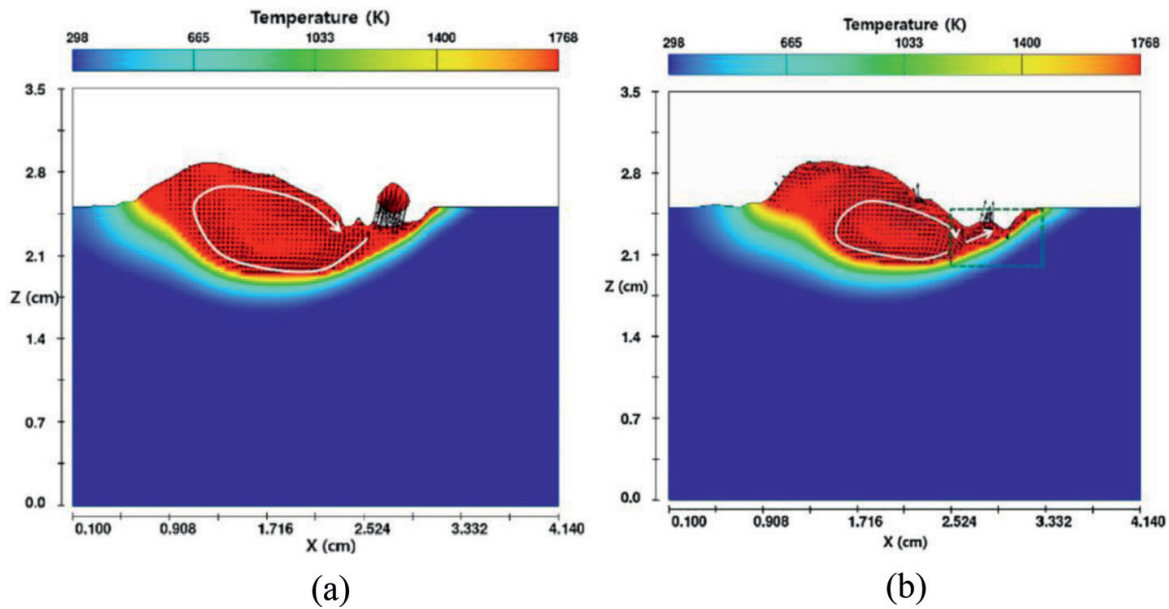


Figure 11. Calculated temperature profiles and flow patterns on a longitudinal cross section for negative electrode angle (-20°C) [15] (a) 0.528 s (b) 0.538 s.

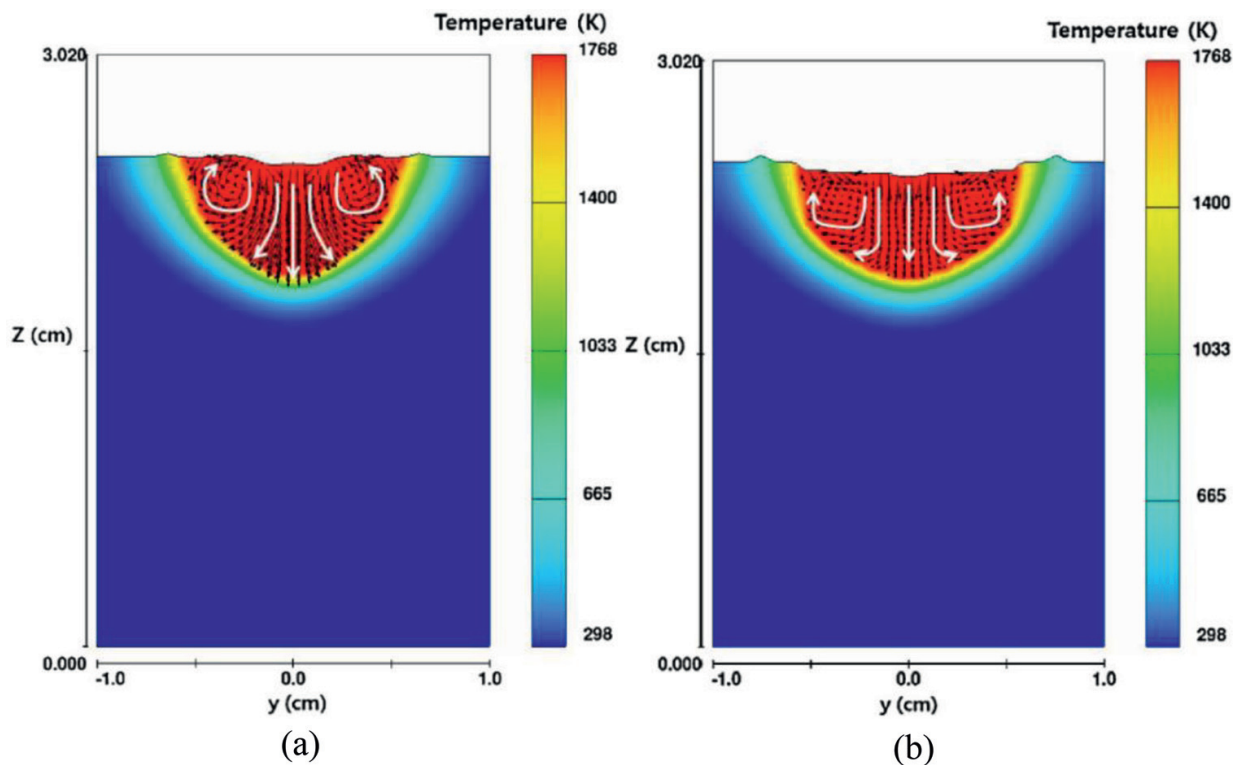


Figure 12. Calculated temperature profiles and flow patterns on a transverse cross section at 0.598 s for negative and positive electrode angle [15] (a) negative angle (-20°) (b) positive angle ($+20^\circ$).

AC welding signals can bring the different simulation results. Cho et al. [15] simulated the molten pool simulation with sinusoidal AC waveform with a negative electrode angle. As the arc shape and signals vary with the welding time, it could induce more dynamic molten pool flows than DC welding. Normally, the frequency of droplet impingement and welding signals cannot be the same so the molten pool under the arc flows forward and backward repeatedly with a welding time as shown in **Figure 14**.

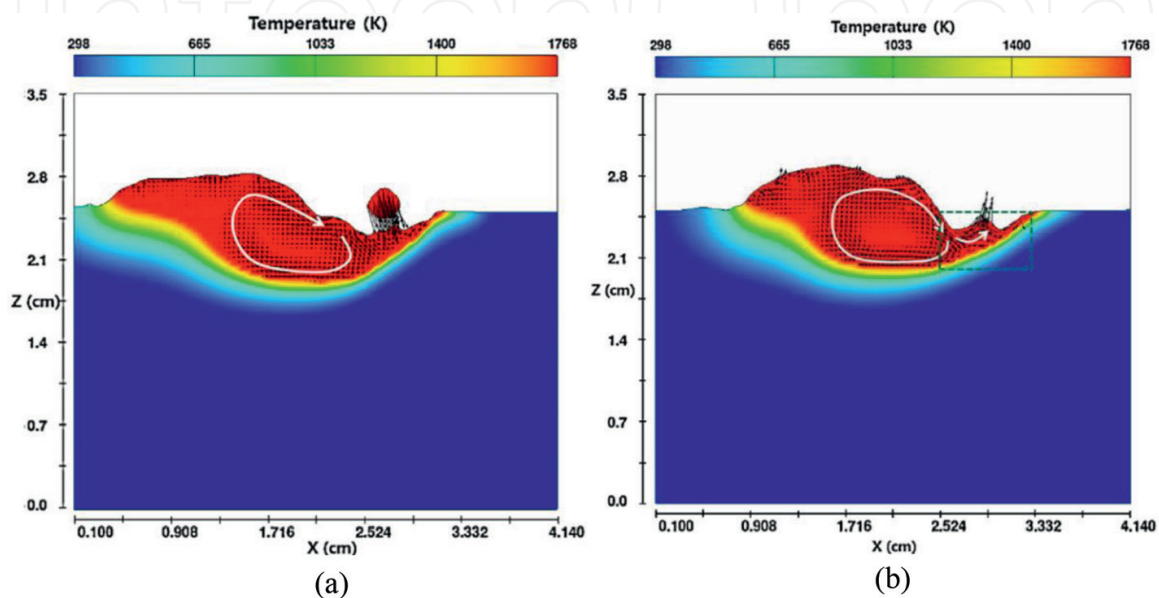


Figure 13. Calculated temperature profiles and flow patterns on a longitudinal cross section for positive electrode angle (+20° C) [15] (a) 0.528 s (b) 0.538 s.

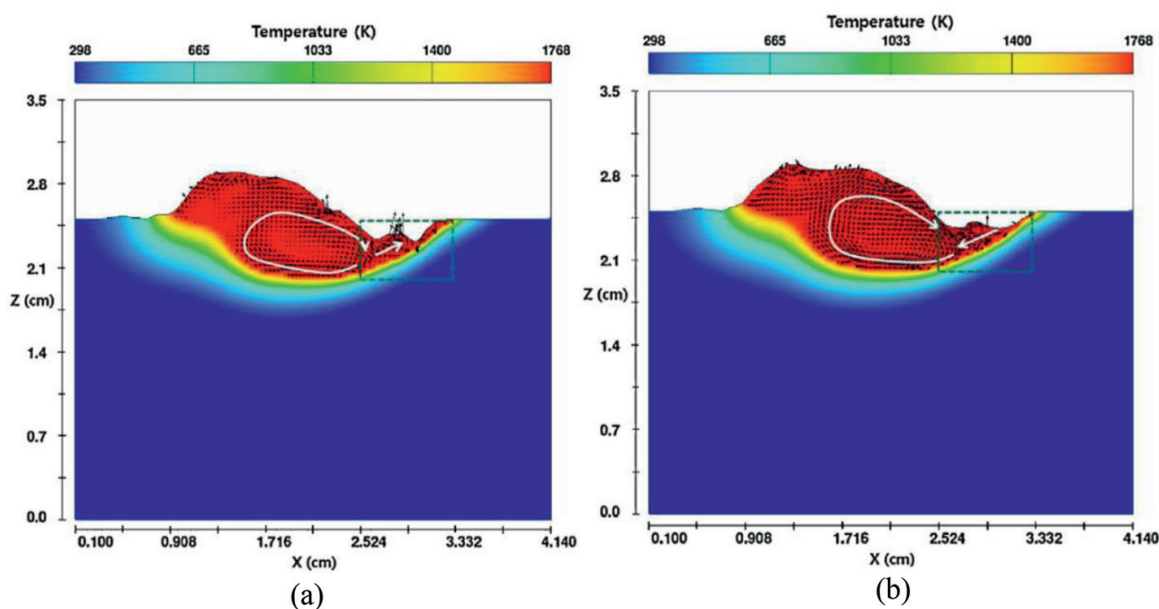


Figure 14. Calculated temperature profiles and flow patterns on a longitudinal cross section for sinusoidal AC waveform (current, voltage) with a negative electrode angle [15] (a) 0.528 s (b) 0.538 s.

When the welding current value is not enough to form the spray metal transfer, it is possible to expect FWG metal transfer mode. Cho et al. [16] simulated the molten pool behavior of FWG metal transfer in V-groove SAW process. The molten droplet impinges to the inner wall boundary and then moves to the V-groove joint sequentially as shown in **Figure 15**. The V-groove joint hardly melts because the arc heat and arc forces (arc pressure & EMF) are not focused on the V-groove joint and. Therefore, it is expected that the inclined side surface melts while the molten pool behavior induces the void in the V-groove joint.

3.2. Multi-wire SAW process

3.2.1. Two wire tandem SAW

Kiran et al. [17] found that when the absolute current value was higher, the arc stiffness increased; thus, the arc tended to be fixed. However, when the absolute current value of the opposite electrode is higher, the arc stiffness decreases, so the arc tends to move backward or forward by the Lorentz force. Finally, the combination of current values from each electrode affects the arc center locations and droplet free flights [18]. For instance, the higher absolute current value can result in an increase in the wire feed rate, which can induce a frequent droplet impingement and a concentration of the arc heat and arc forces.

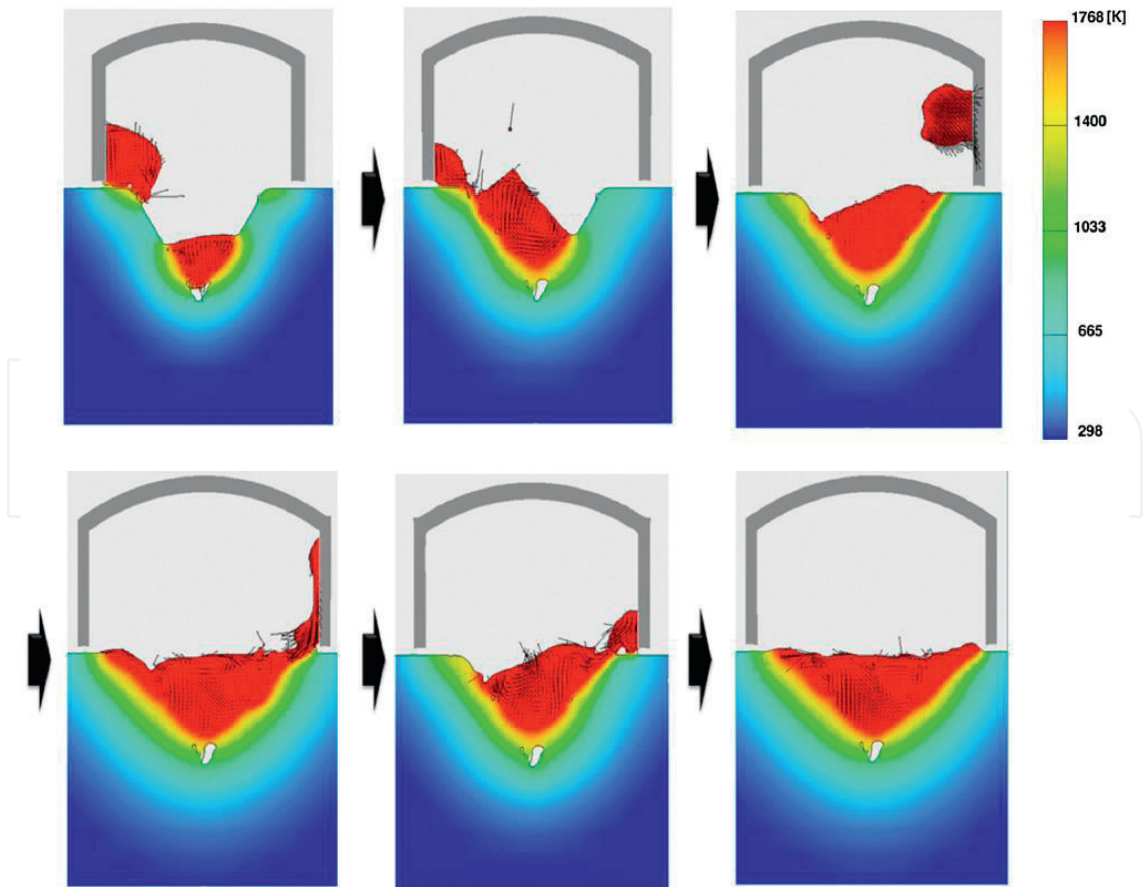


Figure 15. Temperature profiles and flow distributions on the transverse cross section in FWG mode [16].

Using this principle, Cho et al. [18] performed CFD simulations and analyzed the results. For higher current in the leading electrode, the arc center displacement of the leading electrode is very small; moreover, the arc heat, arc force and droplet impingement can be focused under the leading electrode. Therefore, the volume of the molten pool ahead of the leading electrode is very small because droplets do not fly ahead of the leading electrode as shown in **Figure 16(a)**.

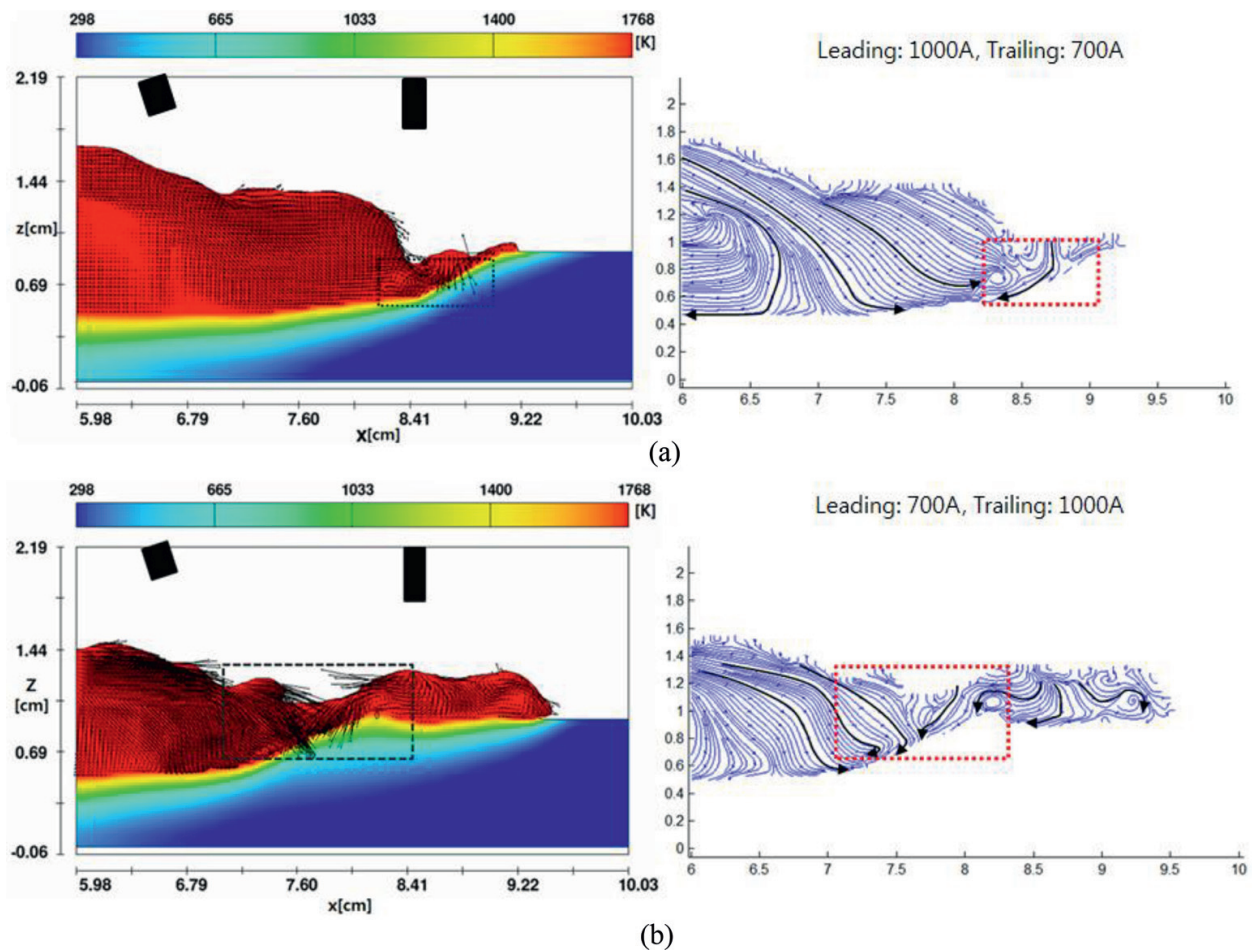


Figure 16. Temperature profiles and streamlines on the longitudinal cross section for two wire tandem SAW process [18] (a) higher current in the leading electrode (b) higher current in the trailing electrode.

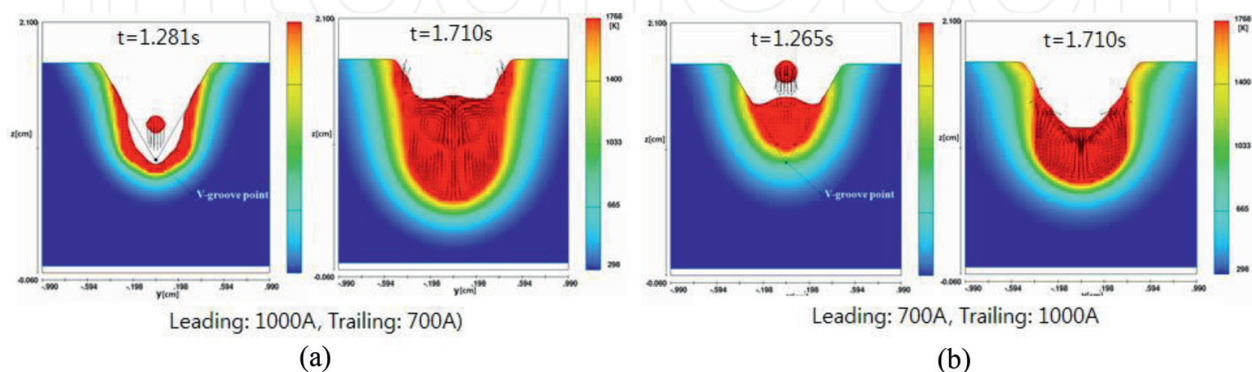


Figure 17. Temperature profiles and streamlines on the transverse cross section for two wire tandem SAW process [18] (a) higher current in the leading electrode (b) higher current in the trailing electrode.

In the transverse section, droplets from the leading electrode impinged on the weld pool whose height is lower than the initial V-groove point; therefore, deep penetration can be from as shown in **Figure 17(a)**. Moreover, the weld pool flows long after droplet impingement in the longitudinal section so this can be another reason to make the deep penetration due to the dynamic convection heat transfer. On the contrary, when the higher current welding signal in the trailing electrode is applied, the arc center displacement of the leading electrode due to the arc

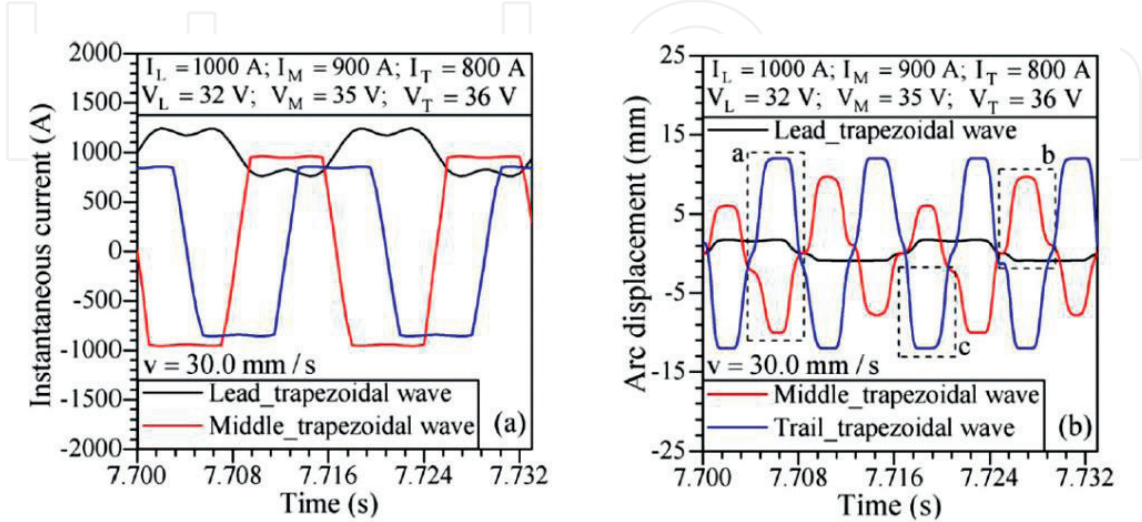


Figure 18. Current waveforms and the corresponding arc center displacement for three wire tandem SAW process [21].

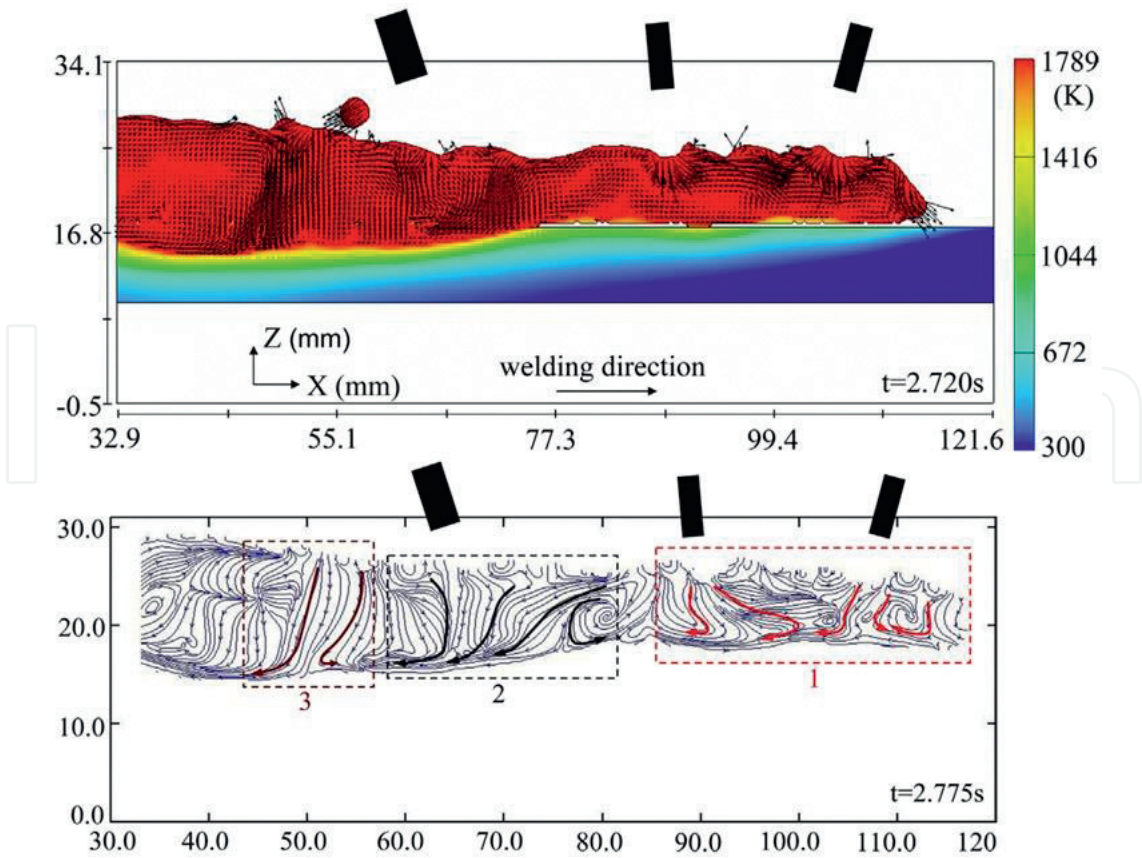


Figure 19. Temperature profiles and streamlines on the longitudinal cross section for three wire tandem SAW process [21].

interaction is much bigger than that of the trailing electrode. Therefore, the droplets, arc heat and arc forces from the leading electrode cannot be focused on a similar weld pool spot, but the droplets disperse forward or backward of the welding direction and the form the volume of the molten pool ahead of the leading electrode as shown in **Figure 16(b)**. With these fluid behaviors, the molten pool can fill in the V-groove point; therefore, the molten pool penetrates to a lesser degree than in the higher current in the leading electrode (**Figure 17(b)**).

3.2.2. Three wire tandem SAW

Kiran et al. [21] modeled and simulated the molten pool flow behavior for three wire tandem SAW in V-groove. They firstly measured welding signals and the arc interaction position of three wire SAW process as shown in **Figure 18** and they found that the molten pool behavior from the arc interaction played an important role to increase the penetration of V-groove. It is evident that the middle and trailing arcs are closely concentrated during the attraction (dotted box 'a') compared to that of the same between leading and middle arcs (dotted box 'b'). When the distances of middle and trailing arcs are short (dotted box 'a'), the focused arc heat and arc forces activate the molten pool behavior more dynamic and these increase penetration in the

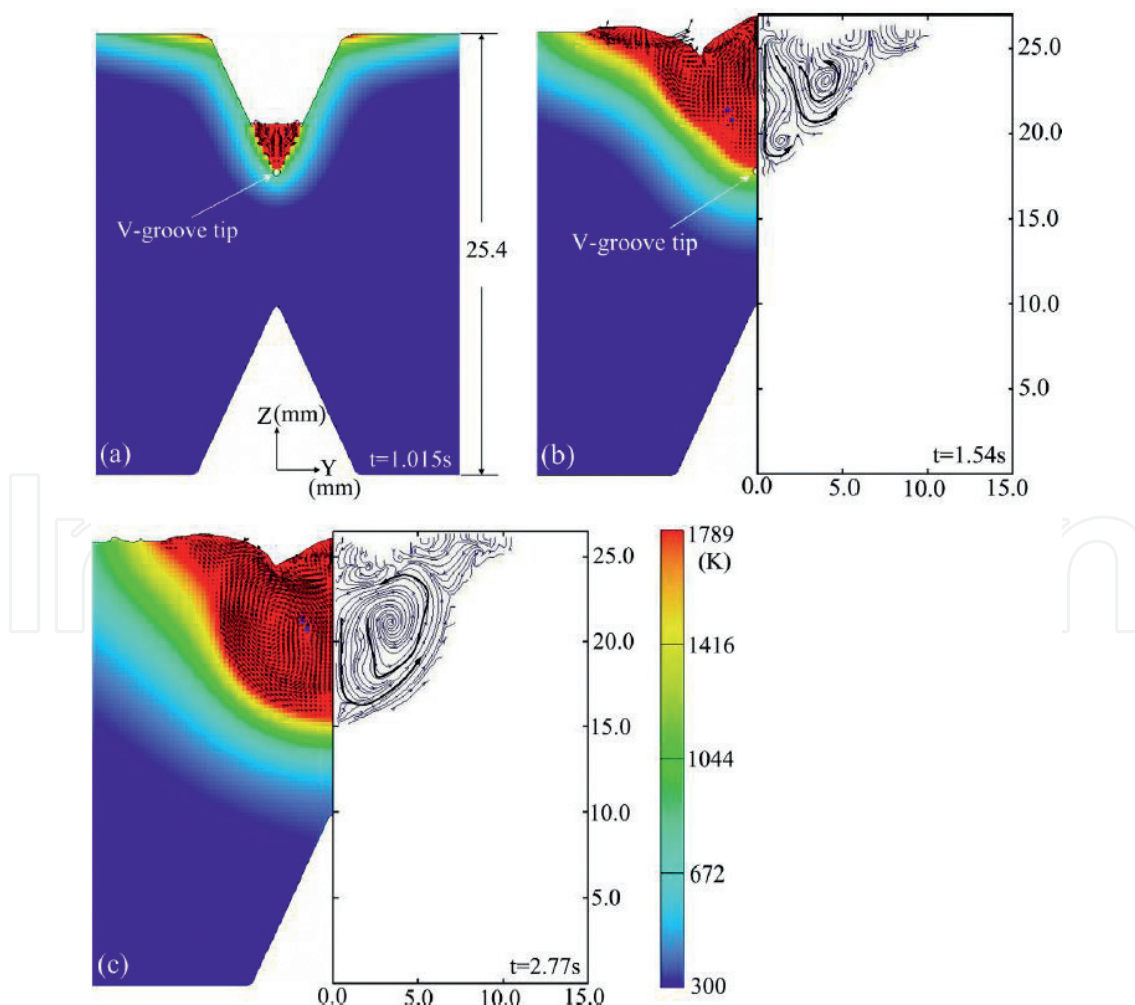


Figure 20. Temperature profiles and streamlines on the transverse cross section for three wire tandem SAW process [21].

longitudinal cross section as shown in **Figure 19**. The molten pool flow patterns in the transverse section are also described in **Figure 20**.

Acknowledgements

The authors gratefully acknowledge the support from Korea Ministry of Trade, Industry and Energy (No.10076430).

Author details

Dae-Won Cho

Address all correspondence to: chodaewon@gmail.com

Busan Machinery Research Center, Korea Institute of Machinery and Materials,
Republic of Korea

References

- [1] Wen SW, Hilton P, Farrugia DCJ. Finite element modelling of a submerged arc welding process. *Journal of Materials Processing Technology*. 2001;**119**(1–3):203-209
- [2] Sharma A, Chaudhary AK, Arora N, Mishra BK. Estimation of heat source model parameters for twin-wire submerged arc welding. *The International Journal of Advanced Manufacturing Technology*. 2009;**45**(11–12):1096
- [3] Mahapatra MM, Datta GL, Pradhan B, Mandal NR. Three-dimensional finite element analysis to predict the effects of SAW process parameters on temperature distribution and angular distortions in single-pass butt joints with top and bottom reinforcements. *International Journal of Pressure Vessels and Piping*. 2006;**83**(10):721-729
- [4] Kiran DV, Basu B, Shah AK, Mishra S, De A. Three-dimensional heat transfer analysis of two wire tandem submerged arc welding. *ISIJ International*. 2011;**51**(5):793-798
- [5] Kim JW, Na SJ. A study on the three-dimensional analysis of heat and fluid flow in gas metal arc welding using boundary-fitted coordinates. *Journal of Engineering for industry*. 1994;**116**(1):78-85
- [6] Kim CH, Zhang W, DebRoy T. Modeling of temperature field and solidified surface profile during gas-metal arc fillet welding. *Journal of Applied Physics*. 2003;**94**(4):2667-2679
- [7] Kim WH, Fan HG, Na SJ. Effect of various driving forces on heat and mass transfer in arc welding. *Numerical Heat Transfer, Part A Applications*. 1997;**32**(6):633-652

- [8] Cho DW, Na SJ, Cho MH, Lee JS. Simulations of weld pool dynamics in V-groove GTA and GMA welding. *Welding in the World*. 2013;**57**(2):223-233
- [9] Cho DW, Na SJ, Cho MH, Lee JS. A study on V-groove GMAW for various welding positions. *Journal of Materials Processing Technology*. 2013;**213**(9):1640-1652
- [10] Cho DW, Lee SH, Na SJ. Characterization of welding arc and weld pool formation in vacuum gas hollow tungsten arc welding. *Journal of Materials Processing Technology*. 2013;**213**(2):143-152
- [11] Cho JH, Na SJ. Implementation of real-time multiple reflection and Fresnel absorption of laser beam in keyhole. *Journal of Physics D: Applied Physics*. 2006;**39**(24):5372
- [12] Cho JH, Na SJ. Three-dimensional analysis of molten pool in GMA-laser hybrid welding. *Welding Journal*. 2009;**88**(2):35-43
- [13] Han SW, Cho WI, Na SJ, Kim CH. Influence of driving forces on weld pool dynamics in GTA and laser welding. *Welding in the World*. 2013;**57**(2):257-264
- [14] Cho WI, Na SJ, Cho MH, Lee JS. Numerical study of alloying element distribution in CO₂ laser-GMA hybrid welding. *Computational Materials Science*. 2010;**49**(4):792-800
- [15] Cho DW, Song WH, Cho MH, Na SJ. Analysis of submerged arc welding process by three-dimensional computational fluid dynamics simulations. *Journal of Materials Processing Technology*. 2013;**213**(12):2278-2291
- [16] Cho DW, Kiran DV, Na SJ. Analysis of molten pool behavior by flux-wall guided metal transfer in low-current submerged arc welding process. *International Journal of Heat and Mass Transfer*. 2017;**110**:104-112
- [17] Kiran DV, Cho DW, Song WH, Na SJ. Arc behavior in two wire tandem submerged arc welding. *Journal of Materials Processing Technology*. 2014;**214**(8):1546-1556
- [18] Cho DW, Kiran DV, Song WH, Na SJ. Molten pool behavior in the tandem submerged arc welding process. *Journal of Materials Processing Technology*. 2014;**214**(11):2233-2247
- [19] Kiran DV, Cho DW, Lee HK, Kang CY, Na SJ. A study on the quality of two-wire tandem submerged arc welds under iso-heat input conditions. *The International Journal of Advanced Manufacturing Technology*. 2015;**78**(1-4):53-62
- [20] Cho DW, Kiran DV, Na SJ. Analysis of the flux consumption and metal transfer for tandem submerged arc welding process under iso-heat input condition. *Welding Journal*. 2015;**94**:396-401
- [21] Kiran DV, Cho DW, Song WH, Na SJ. Arc interaction and molten pool behavior in the three wire submerged arc welding process. *International Journal of Heat and Mass Transfer*. 2015;**87**:327-340
- [22] Franz U. Vorgänge in der Kaverne beim UP-Schweissen Teil I. *Schweiss Tech*. 1965;**15**:145-150
- [23] Van Adrichem JT. Metal transfer in submerged arc welding. *International Institute of Welding Document*. 1966:212-278

- [24] Chandel RS. The effect of process variables on the flux consumption in submerged arc welding. *Material and Manufacturing Process*. 1998;**13**(2):181-188
- [25] Renwick BG, Patchett BM. Operating characteristics of the submerged arc process. *Welding Journal*. 1976;**55**(3):69
- [26] Kou S, Sun DK. Fluid flow and weld penetration in stationary arc welds. *Metallurgical Transactions A*. 1985;**16**(1):203-213
- [27] Sahoo P, DebRoy T, McNallan MJ. Surface tension of binary metal—Surface active solute systems under conditions relevant to welding metallurgy. *Metallurgical Transactions B*. 1988;**19**(3):483-491
- [28] Cho DW. A Study on Molten Pool Flow Behavior in Pipe Seam Welding and Girth Welding Processes by Computational Fluid Dynamics. Kaist Ph. D [Thesis] 2014

IntechOpen